Renewable Energy 210 (2023) 280–294

Contents lists available at ScienceDirect

Renewable Energy

journal homepage: www.elsevier.com/locate/renene

Mathematical modelling of a floating Clam-type wave energy converter

Siming Zheng *, John Wilfrid Phillips, Martyn Hann, Deborah Greaves

School of Engineering, Computing and Mathematics, University of Plymouth, Drake Circus, Plymouth PL4 8AA, UK

ARTICLE INFO

Keywords:
Wave–structure interaction
Potential flow theory
Clam-type wave energy converter
Boundary element method
Generalised mode method
Flexible device

ABSTRACT

In this paper, wave power extraction from a floating Clam-type wave energy converter is investigated. The device is mainly composed of a Clam, which is formed from two pieces of floating flaps hinged at a submerged body. The Clam is closed by a flexible impermeable bag with the two hinged floating flaps kept apart by a Power Take-Off system. As waves propagate through the device, the Clam motion of the device is excited, which can be used to drive the Power Take-Off system to capture wave power. To evaluate the response and also the wave power absorption of the device, a mathematical model is developed based on the linear potential flow theory, in which a generalised mode method is adopted to model the Clam action. Theoretical expressions of the maximum wave power absorption and the corresponding optimised Power Take-Off system and mooring parameters are derived. Good agreement between the present numerical results of the device response and the physical observations is obtained. The validated model is then applied to do a series of case studies. It is revealed that the optimised Power Take-Off stiffness and mooring stiffness are independent of the Power Take-Off damping. The maximum wave power absorption can be achieved when the device is fixed in heave mode or free-floating without any constraints from the mooring system.

1. Introduction

To capture wave power from ocean waves, a large number of wave energy conversion concepts have been proposed since the 1790s [1]. In spite of the large variation in concepts and design, most of them are composed of rigid floats (e.g., see [2–5]). Apart from the traditional rigid floats based wave energy converters (WECs), a flexible deformable body can work as a WEC as well. Its mean shape can be changed so as to adjust its resonant periods, adapting itself to different environmental conditions, e.g., the sea sites where wave conditions change seasonally from summer to winter. A flexible deformable structured WEC is also expected to have a better survivability in extreme wave conditions [6].

The Lancaster Flexible Bag and Circular Clam developed in the early 1980s could be the first flexible WECs [7]. The devices are composed of a series of inflatable bags filled with air. The air bags would expand and contract following the oscillatory motion of the incoming waves, pumping air into a turbine connected to a generator. A similar technique is also adopted in the mWave WEC developed by the company Bombora Wave Power [8]. Anaconda and S3 are two attenuator-type flexible WECs consisting of a long submerged elastic tube filled with water [9,10]. Bulge waves propagating along the tube can be excited by the interaction between water waves and the flexible tube. The bulge waves then derive a power take-off system at the stern or distributed along the tube, e.g., electro-active polymers, to capture electricity. The Wave Carpet developed at UC Berkeley in 2012 is composed of a flexible elastic plate submerged under the water [11]. The deformation of the plate drives a series of cylinders installed between the plate and the sea bed to capture wave power. This concept was later extended to a floating plate-shaped flexible WECs, the hydrodynamic performance of which was studied by Michele et al. [12,13] and Zheng et al. [14] theoretically. A comprehensive overview of the current state of the flexible structure-based wave energy conversion technology is given by Collins et al. [6] and Renzi et al. [15].

The floating Clam-type wave energy converter (C-WEC) proposed by Farley [16] is another typical flexible deformable WEC, which consists of a pair of flaps that are hinged at the bottom. The clam is closed by inextensible polymer-coated fabric, resulting in a pressurised bag to hold the hinged clam sides apart, giving a V-shaped cross-section. As ocean waves propagate through the device, the clam opens and shuts and, meanwhile, the air is pumped into and out of a second closed vessel above the clam via a turbine/generator set, achieving wave power absorption. A preliminary analysis of the hydrodynamic performance and cost estimate were presented by Farley [16], demonstrating a competitive cost (capital cost 3400 GBP per kW) for a machine with 100 kW averaged power output. Since the free floating clam is entirely sealed, it may have challenges for manufacturing and maintenance. Later, Phillips et al. [17] and Phillips [18] carried out both physical tests and numerical investigation of a floating Clam-type WEC equipped with an alternative mechanical power take-off

* Corresponding author.
E-mail address: siming.zheng@plymouth.ac.uk (S. Zheng).

https://doi.org/10.1016/j.renene.2023.04.040
Received 24 August 2022; Received in revised form 1 April 2023; Accepted 11 April 2023
Available online 17 April 2023

Nomenclature

$(x_{0\pm}, z_0)$	Positions of the two hinges in the Oxz plane ([m], [m])
$\bar{c}_{PTO}$, $\bar{k}_{PTO}$, $\bar{k}_m$	Nondimensionalised PTO damping, PTO stiffness and mooring stiffness
η	Wave energy capture width ratio (or capture factor) [–]
$\mathbf{C_{PTO}}$, $\mathbf{K_{PTO}}$	PTO system associated damping and stiffness matrices, respectively
$\mathbf{M_a}$, $\mathbf{C_d}$	Matrices of added-mass and wave radiation damping coefficients, respectively
$\mathbf{M}$, $\mathbf{K_s}$	Matrices of the device mass and static stiffness, respectively
ω	Angular frequency of incident waves [rad/s]
Φ	Total flow velocity potential [m^2/s]
ϕ	Spatial flow velocity potential [m^2/s]
ϕ_D	Velocity potential of diffracted waves [m^2/s]
ϕ_I	Velocity potential of undisturbed incident waves [m^2/s]
ϕ_j	Velocity potential of radiated waves induced by oscillation of the device in Mode j with unit velocity amplitude
ρ	Density of the water [kg/m^3]
θ	Opening angle of each flap when the device is at equilibrium [rad]
θ_0	Opening angle of each flap when no resistance is provided by the PTO stiffness [rad]
$\boldsymbol{\xi}$, $\boldsymbol{F_e}$	Vectors of the device displacement and wave excitation forces, respectively
$\vec{n}$	Unit normal on the wetted surface of the device directed away from the fluid domain, $\vec{n} = (n_x, n_y, n_z)$
A	Amplitude of incident waves [m]
b	Width of the device [m]
$c_{i,j}$, $m_{i,j}$	Radiation damping and added mass, respectively, of Mode i due to the motion in Mode j
c_{PTO}, k_{PTO}	Damping [N m s] and stiffness [N m], respectively, of the PTO system
d	Submerged depth of the flaps [m]
f_3, f_7	Heave excitation force [N] and Clam excitation moment [N m], respectively
$F_{m,0}$	Mooring force acting on the device in still water [N]
g	Gravitational acceleration [m/s^2]
h	Water depth [m]
I	Rotary inertia of each flap about the hinge [kg m^2]
k	Wave number [m^{-1}]
k_m	Stiffness of the mooring system [N/s]
l	Length of the flaps [m]
M_0	Constant moment acting on each flap provided by a constant force spring [N m]
m_0	Mass of each flap [kg]
M_s	Moment acting on each flap provided by the PTO spring [N m]
m_s	Total mass of the device with the two flaps excluded [kg]
$Oxyz$	Cartesian coordinate system
P	Time-averaged wave power captured by the device [W]
P_{in}	Incident wave power per unit width of the wave front [W]
P_{MAX}	Maximum absorbed wave power when the PTO damping, PTO stiffness and mooring stiffness are all optimised [W]
$P_{max}^{c,k}$	Maximum absorbed wave power when the PTO damping and PTO stiffness are both optimised [W]
$P_{max}^{c,m}$	Maximum absorbed wave power when the PTO damping and mooring stiffness are both optimised [W]
P_{max}^{c}, c_{opt}	Maximum absorbed wave power [W] and the corresponding optimised PTO damping [N m s]
$P_{max}^{k,m}$	Maximum absorbed wave power when the PTO stiffness and mooring stiffness are both optimised [W]
P_{max}^{k}, k_{opt}	Maximum absorbed wave power [W] and the corresponding optimised PTO stiffness [N m]
P_{max}^{m}	Maximum absorbed wave power when the mooring stiffness is optimised [W]
S	Total area of the cut water-plane [m^2]
t	Time [s]
t_0	Thickness of the flap [m]
z_j, ξ_j	Instantaneous displacement and time-independent amplitude of displacement, respectively, of each flap in Mode j

(PTO) system, which is composed of hydraulic rams and tension springs holding the Clam sides apart. The Clam motion was treated as a generalised mode in their numerical model. For simplicity, the flap was assumed to be weightless in the analysis adopted in the frequency domain. The Clam was found to be most effective when the device was constrained in heave. More recently, Kurniawan et al. [19] turned their attention to an axisymmetric version of the floating device, in which the pair of rigid plates is replaced by a completely flexible bag. The static and dynamic behaviour of the device was investigated numerically and experimentally. The results showed that the bag shape and dynamic response could be changed by varying the amount of air in the bag. The dynamic response, but not the shape, also depended on the turbine damping. The resonance period of the device was found to be larger than that of a rigid device with the same geometry. An accompanied loss in bandwidth compared to the bandwidth of the rigid device, albeit not severe, was observed. Kurniawan et al. [20] proposed another variation of the device by arranging the flexible bag to be fully submerged and connected to a rigid ballasted float at the top and to a weighted cylinder at the bottom. Three different equilibrium device geometries were indicated in their study for the same bag pressure.

Although the wave power extraction of different versions of the floating clam device have been investigated both numerically and experimentally, most of them have been focused on examining the performance of the device with an arbitrarily specified PTO damping, and the optimisation of their PTO for maximising power absorption has not been carried out. The aim of the present work is, therefore, to develop a mathematical model to seek the maximum wave power that can be captured by a floating clam device, and specify the corresponding optimised PTO/mooring system required theoretically. The model is then applied to study the performance of the device with different geometrical parameters.

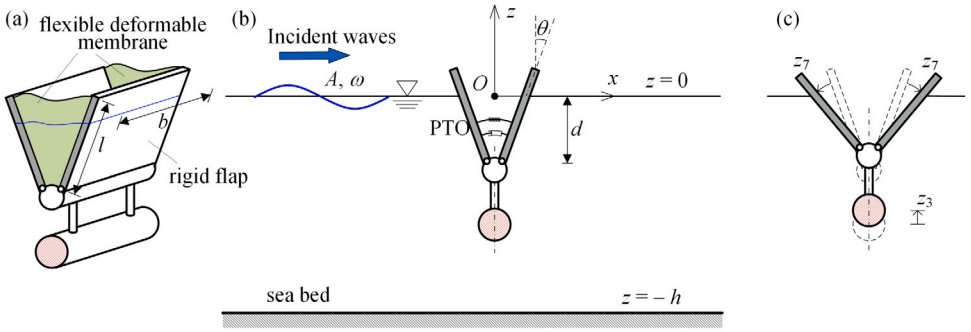

Fig. 1. Schematic diagram of a C-WEC: (a) isometric view; (b) side view in still water; (c) definition of heave motion and Clam motion.

The remainder of the paper is structured as follows. The mathematical model for the wave–structure interaction problem is described in Section 2. The expressions of the theoretical maximum wave power absorption, together with the corresponding optimised PTO parameters can be found in Section 3. The present model is validated by comparing the present results with measured physical data, and the validated model is applied to carry out a multi-parameter study on the performance of C-WEC, the results of which, together with discussions, are also presented in Section 4. Finally, conclusions are drawn in Section 5.

2. Mathematical model

Fig. 1 shows the schematic diagram of the problem. The C-WEC device consists of two rigid flaps, which are flexibly connected to two hinges at a submerged body and held apart by a PTO system. The flexible parts of the device are made from waterproof flexible deformable membranes, which allow the two flaps to freely rotate about the hinges. A potential benefit of the flexible parts is the possibility to integrate an alternative PTO system, e.g., a dielectric elastomer generator (DEG) [21], into it, helping reduce the amount of mechanical moving parts and ensure reliability and reduced/simplified maintenance costs of the device. Yet this is out of the scope of the present paper. The tension and deflection of the membranes are assumed to be small and neglected in the hydrodynamic problem. However, for the C-WEC of small width, the tension and deflection of the membranes may become much more significant and may have to be taken into account. A Cartesian coordinate system $Oxyz$ is adopted with the mean free-surface coinciding with the Oxy-plane, the Oyz-plane coinciding with symmetric plane of C-WEC, and z measured vertically upwards. Therefore, the fluid bottom (i.e., the sea bed) is at $z = -h$. The dimension of the device in the y-direction, i.e., the width, is denoted by b. The length and the submerged depth of each flap are denoted by l and d, respectively. The C-WEC is subjected to regular waves of angular frequency ω and amplitude A, propagating along the Ox-axis.

The motion of the C-WEC can be decomposed into 7 modes. The first 6 modes are the conventional rigid body modes. Modes 1 to 3 describe translational motion in the x, y, z (surge, sway and heave) axes, respectively, and Modes 4, 5 and 6 represent rotation about the x, y, and z axes (roll, pitch and yaw), respectively. Mode 7 is a 'generalised mode', i.e., the Clam mode, and it is defined by the movement of the PTO ram — the positive direction of movement being shown by the arrows as shown in Fig. 1c. This definition of the Clam mode is different from that adopted by Phillips [18], who defined the Clam mode as unit change of the distance between the two flaps along the line of action of PTO. Different definitions of the Clam mode would result in different hydrodynamic coefficients and different Clam mode related generalised mass and restoring stiffness, and PTO parameters as well.

For regular incident waves propagating along the Ox-axis, only surge, heave, pitch, and Clam modes are excited provided the $y = 0$ is a plane of symmetry for both geometries and physical properties of the C-WEC. The present work is focused on the responses in heave and Clam modes, since the Clam mode is associated with wave power absorption of the C-WEC and coupled with the heave mode. Although the motions of the C-WEC in surge and pitch modes do exist, they are not considered hereinafter because they are decoupled with the heave and Clam modes.

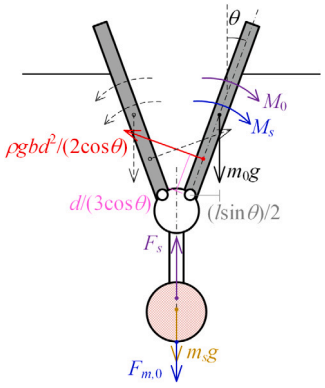

Fig. 2. Schematic diagram of static force analysis.

2.1. Static shape of C-WEC

The static shape of the Clam in terms of θ (the opening angle between the two flaps is 2θ), together with the device position in terms of d (see Fig. 1b), should be evaluated prior to the hydrodynamic analysis. Fig. 2 presents a schematic diagram of static force/moment acting on the device in still water. M_s denotes the moment acting on the flap provided by the compressed spring in the PTO system with $M_s = -2k_{PTO}(\theta - \theta_0)$, in which k_{PTO} is the stiffness of the PTO system and θ_0 represents the Clam position (i.e., the opening angle between the two flaps is $2\theta_0$) when no resistance is provided by the PTO stiffness; m_0 is the mass of each flap; m_s represents the total mass of the device with the two flaps excluded; F_s denotes the net vertical buoyancy force due to the hydrostatic pressure acting on the wetted surface of the whole device except the two flaps; ρ is the density of the water, and g represents the gravitational acceleration. M_0 and $F_{m,0}$ represent a constant moment acting on the flap, which could be provided by using a constant force spring, and the mooring force acting on the device in still water, respectively, and they can be used to adjust the static shape of C-WEC.

For a C-WEC placed at its equilibrium in still water, the following two relations should be satisfied:

- The overall buoyancy of the device equals the weight of the device, and the mooring force

$$\rho g b d^2 \tan\theta + F_s - (2m_0 + m_s)g - F_{m,0} = 0. \tag{1}$$

- The buoyancy-moment acting on the two flaps about the hinges is equal to two times the moment induced by the PTO system, the weight of the flap and the constant force spring

$$\begin{aligned} &2(M_s + M_0) + m_0\ gl\sin\theta - \frac{\rho g b (d + t_0/2\sin\theta)^3}{3\cos^2\theta} \\ \approx &2(M_s + M_0) + m_0\ gl\sin\theta - \frac{\rho g b d^3}{3\cos^2\theta} = 0, \end{aligned} \tag{2}$$

where t_0 represents the thickness of the flap, which is assumed to be much smaller than d.

It is noted that both θ and d are unknown, nevertheless, they are dependent on each other, i.e., once one of them is known, the other one can be evaluated accordingly. θ can be evaluated iteratively with a bisection method by assuming an initial value between 0 and $\pi/2$ and solving for the corresponding d, until the computed value of d is close to the target value within a given tolerance.

2.2. Dynamic model

All amplitudes are assumed to be small enough that linear theory applies, and the fluid is assumed to be inviscid, incompressible and irrotational. It is further assumed that all motion is time-harmonic with angular frequency ω, hence the fluid velocity potential and the displacement of the C-WEC about its static equilibrium position may be expressed by

$$\Phi(x, y, z, t) = \mathrm{Re}\{\phi(x, y, z)\mathrm{e}^{\mathrm{i}\omega t}\}, \tag{3}$$

and

$$z_j(t) = \mathrm{Re}\{\xi_j \mathrm{e}^{\mathrm{i}\omega t}\}, \quad \text{for } j = 3, 7, \tag{4}$$

where Re denotes the real part. The functions $\phi(x, y, z)$ and ξ_j represent the time-independent parts of the complex velocity potential and the complex displacement of the device in Mode j, respectively.

Under the assumptions above, the spatial velocity potential satisfies the Laplace equation in the fluid with the boundary conditions

$$\frac{\partial \phi}{\partial z} = \frac{\omega^2}{g}\phi \quad \text{on} \quad z = 0, \tag{5}$$

$$\frac{\partial \phi}{\partial z} = 0 \quad \text{on} \quad z = -h, \tag{6}$$

$$\frac{\partial \phi}{\partial n} = \mathrm{i}\omega(\xi_3 n_3 + \tau\xi_7 n_7) \quad \text{on the mean wetted surface of the device} \tag{7}$$

where $\partial/\partial n = \vec{n}\cdot\nabla$, in which $\vec{n}$ represents the unit normal on the boundary curve directed away from the fluid domain. $n_3 = n_z$ and $n_7 = (z - z_0)n_x - (x - x_0)n_z$, in which n_x and n_z are the components of $\vec{n}$ in x and z dimensions, respectively; x_0 and z_0 denote the position of the hinge point of the flaps in x and z dimensions. For the device with the two flaps hinged together at an identical hinge, we have $x_0 = 0$. Otherwise, if the flaps are allowed to rotate about two symmetrically deployed hinges separately rather than about the identical hinge, x_0 will be split into x_{0^-} and x_{0^+}, which correspond to the horizontal position of the two flap hinges, with $x_{0^-} + x_{0^+} = 0$ and $x_{0^+} > 0$. $\tau = 1$ and -1 for the wetted surface of the right-hand side flap and the left-hand side one (see Fig. 1), respectively, and $\tau = 0$ for the other wetted part of the device.

2.3. Hydrodynamic solutions

The velocity potential in the fluid domain can be further decomposed into incident wave, diffracted wave and radiated wave components as follows

$$\phi = \phi_I + \phi_D + \mathrm{i}\omega\xi_3\phi_3 + \mathrm{i}\omega\xi_7\phi_7, \tag{8}$$

where ϕ_I is the velocity potential of undisturbed incident waves; ϕ_D represents the velocity potential of the diffracted wave due to the existence of the fixed device; ϕ_3 and ϕ_7 are the radiated velocity potentials induced by oscillation of the device in heave and Clam modes, respectively, with unit velocity amplitude. ϕ_D, ϕ_3 and ϕ_7 can be determined with the employment of a boundary element method (BEM)-based numerical code, e.g., WAMIT [22] and NEMOH [23].

3. Response and wave power absorption of the C-WEC

3.1. Motion response

The motion response matrix equation of the C-WEC may be expressed as

$$[-\omega^2(\mathbf{M} + \mathbf{M_a}) + \mathrm{i}\omega(\mathbf{C_d} + \mathbf{C_{PTO}}) + \mathbf{K_s} + \mathbf{K_{PTO}} + \mathbf{K_m}]\boldsymbol{\xi} = \boldsymbol{F_e}, \tag{9}$$

in which $\mathbf{M}$ and $\mathbf{K_s}$ are the matrices of the device mass and static stiffness, respectively; $\mathbf{M_a}$ and $\mathbf{C_d}$ represent the matrices of added-mass and wave radiation damping coefficients, respectively; $\mathbf{C_{PTO}}$ and $\mathbf{K_{PTO}}$ are the PTO system associated damping and stiffness matrices, respectively; $\mathbf{K_m}$ represents the stiffness matrix of the mooring system; $\boldsymbol{\xi} = [\xi_3, \xi_7]^T$ and $\boldsymbol{F_e} = [f_3, f_7]^T$ represent the vector of the displacements of the device and the vector of the wave excitation forces acting on the device in heave mode and Clam mode, respectively. $\mathbf{M_a}$, $\mathbf{C_d}$ and $\boldsymbol{F_e}$ can be obtained by using a BEM-based code. The specific expressions of the matrices at the left-hand side of Eq. (9) are given as follows:

$$\mathbf{M} = \begin{bmatrix} m_{3,3}^{(0)} & m_{3,7}^{(0)} \\ m_{7,3}^{(0)} & m_{7,7}^{(0)} \end{bmatrix} \approx \begin{bmatrix} m & -m_0 l\sin\theta \\ -m_0 l\sin\theta & 2I \end{bmatrix}, \tag{10}$$

$$\mathbf{K_s} = \begin{bmatrix} k_{3,3} & k_{3,7} \\ k_{7,3} & k_{7,7} \end{bmatrix} \approx \begin{bmatrix} \rho g S & -\frac{\rho g b d^2}{\cos^2\theta} \\ -\frac{\rho g b d^2}{\cos^2\theta} & \frac{2\rho g b d^3\tan\theta}{3\cos^2\theta} - m_0\ gl\cos\theta \end{bmatrix}, \tag{11}$$

$$\mathbf{C_{PTO}} = \begin{bmatrix} c_h & 0 \\ 0 & 4c_{PTO} \end{bmatrix}, \tag{12}$$

$$\mathbf{K_{PTO}} = \begin{bmatrix} 0 & 0 \\ 0 & 4k_{PTO} \end{bmatrix}, \tag{13}$$

$$\mathbf{K_m} = \begin{bmatrix} k_m & 0 \\ 0 & 0 \end{bmatrix}, \tag{14}$$

$$\mathbf{M_a} = \begin{bmatrix} m_{3,3} & m_{3,7} \\ m_{7,3} & m_{7,7} \end{bmatrix}, \tag{15}$$

$$\mathbf{C_d} = \begin{bmatrix} c_{3,3} & c_{3,7} \\ c_{7,3} & c_{7,7} \end{bmatrix}, \tag{16}$$

in which S represents the total area of the cut water-plane; k_m is adopted to consider the effect of the stiffness induced by a mooring system linking the submerged float to the seabed; $m = 2m_0 + m_s$, $I = m_0 l^2/3$ is the rotary inertia of each flap about the hinge; c_{PTO} is the damping coefficient of the PTO system; c_h denotes the external heave damping coefficient, which vanishes unless otherwise specified; $m_{i,j}$ and $c_{i,j}$ for $i, j = 3, 7$ represent the hydrodynamic coefficients of Mode i due to the motion in Mode j. It should be noted that the heave and Clam modes are not only coupled in terms of hydrodynamic coefficient matrices $\mathbf{M_a}$ and $\mathbf{C_d}$, but also with regard to the matrices of the device mass and static stiffness, i.e., $\mathbf{M}$ and $\mathbf{K_s}$, the detailed derivation of the expressions are given in Appendix. The total clam opening angle change ($2\xi_7$) may be a natural parameter for a Clam with a single hinge, but the present device has two separate hinges, so the individual opening angle change (ξ_7) is used here in defining the generalised mode. Therefore the PTO damping and PTO stiffness in Eqs. (12) and (13) read $4c_{PTO}$ and $4k_{PTO}$, respectively, because they are related to the rates of change of PTO moment with total clam opening angle change $2\xi_7$.

$$P^{c}_{max} = \frac{1}{4}\frac{\omega|(A_0+k_m)f_7 - C_0 f_3|^2}{|A_0+k_m||(A_0+k_m)(D_0+4k_{PTO}) - B_0C_0| - \mathrm{Im}\{(A_0+k_m)[(A_0+k_m)^* D_0^* - B_0^* C_0^*]\}}. \tag{22}$$

Box I.

3.2. Wave power absorption

Wave power is converted by the damping effect of the PTO system. The time-averaged power that C-WEC captures from regular waves can be written as

$$P = \frac{1}{2}c_{PTO}\omega^2|2\xi_7|^2 = 2c_{PTO}\omega^2|\xi_7|^2. \tag{17}$$

The wave energy capture width ratio (or capture factor) can be calculated by

$$\eta = \frac{P}{bP_{\mathrm{in}}} = \frac{4kP}{b\rho g A^2\omega[1+\frac{2kh}{\sinh(2kh)}]}, \tag{18}$$

where P_{in} represents the incident wave power per unit width of the wave front, and k denotes the wave number.

3.3. Maximum wave power absorption

The subject of this subsection is to study, theoretically, the maximum wave power that the C-WEC can capture from regular water waves. Optimisation of three variables, i.e., PTO damping, PTO stiffness, and mooring stiffness, are considered.

In order to derive the expressions of the maximum wave power absorption, together with the corresponding optimised parameters, the variables should be separated and the motion equation may be rewritten as

$$\begin{bmatrix} A_0+k_m & B_0 \\ C_0 & D_0+4k_{PTO}+4\mathrm{i}\omega c_{PTO}\end{bmatrix}\begin{Bmatrix}\xi_3\\ \xi_7\end{Bmatrix} = \begin{Bmatrix} f_3\\ f_7\end{Bmatrix}, \tag{19}$$

where the subscript "0" denotes the element is independent of both the PTO parameters and the stiffness of mooring system, $A_0 = k_{3,3} - \omega^2(m+m_{3,3}) + \mathrm{i}\omega c_{3,3}$, $B_0 = k_{3,7} - \omega^2(m_{3,7} - m_0 l\sin\theta) + \mathrm{i}\omega c_{3,7}$, $C_0 = k_{7,3} - \omega^2(m_{7,3} - m_0 l\sin\theta) + \mathrm{i}\omega c_{7,3}$, $D_0 = k_{7,7} - \omega^2(2I + m_{7,7}) + \mathrm{i}\omega c_{7,7}$.

Correspondingly, the time-averaged wave power absorption can be expressed as

$$P = \frac{2|(A_0+k_m)f_7 - C_0 f_3|^2\omega^2 c_{PTO}}{|(A_0+k_m)(D_0+4k_{PTO}+4\mathrm{i}\omega c_{PTO}) - B_0C_0|^2}. \tag{20}$$

For the device in a specified sea state, three parameters, i.e., PTO damping (c_{PTO}), PTO stiffness (k_{PTO}), and mooring stiffness (k_m), could be optimised to improve the performance of the device in wave power absorption. Hereinafter, three different levels of optimisation principles are considered, i.e., levels I, II, and III. For level I optimisation, two of these three parameters are fixed with given values, and the remaining one is optimised. For the level II optimisation, one of them is fixed with a specified value, and the remaining two are optimised at the same time. For the level III optimisation, all these three parameters are optimised at the same time.

(1) Level I, optimisation of c_{PTO}

There is a corresponding maximum of absorbed wave power when $\frac{\partial P}{\partial c_{PTO}} = 0$, which occurs if

$$c_{PTO} = \frac{|(A_0+k_m)(D_0+4k_{PTO}) - B_0C_0|}{4|A_0+k_m|\omega} \equiv c_{opt}, \tag{21}$$

where the subscript "opt" denotes optimisation of PTO damping.

The maximum absorbed wave power with c_{opt} can be further expressed as (see Eq. (22) which is given in Box I).

(2) Level I, optimisation of k_{PTO}

There is a corresponding maximum of absorbed wave power when $\frac{\partial P}{\partial k_{PTO}} = 0$, which occurs if

$$k_{PTO} = -\frac{1}{4}\mathrm{Re}\left\{D_0 - \frac{B_0C_0}{A_0+k_m}\right\} \equiv k_{opt}, \tag{23}$$

which indicates that the optimised PTO stiffness is affected by the stiffness of the mooring system, but independent of the PTO damping coefficient.

The maximum absorbed wave power with k_{opt} can be further expressed as

$$P^{k}_{max} = \frac{2|(A_0+k_m)f_7 - C_0f_3|^2\omega^2 c_{PTO}}{|A_0+k_m|^2\left(\mathrm{Im}\left\{D_0 - \frac{B_0C_0}{A_0+k_m}\right\} + 4\omega c_{PTO}\right)^2}. \tag{24}$$

A negative-stiffness mechanism is common in some control strategies of WECs, e.g., the reactive phase control strategy (e.g., see [24]). The negative-stiffness may be achieved by using some well-arranged classic positive-stiffness springs, e.g., two symmetrical oblique springs [25,26], or by adopting magnetic springs (e.g., see [27,28]). Nevertheless, the application of a negative-stiffness mechanism would increase the complexity of the device and may affect the stability as well. In the present work, the PTO stiffness is assumed to be non-negative. Hence, Eqs. (23) and (24) may be rewritten as:

$$k_{opt} = \begin{cases} 0, & \mathrm{Re}\left\{D_0 - \frac{B_0C_0}{A_0+k_m}\right\} \geq 0 \\ -\frac{1}{4}\mathrm{Re}\left\{D_0 - \frac{B_0C_0}{A_0+k_m}\right\}, & \mathrm{Re}\left\{D_0 - \frac{B_0C_0}{A_0+k_m}\right\} < 0, \end{cases} \tag{25}$$

and

$$P^{k}_{max} = \begin{cases} \frac{2|(A_0+k_m)f_7 - C_0f_3|^2\omega^2 c_{PTO}}{|(A_0+k_m)(D_0+4\mathrm{i}\omega c_{PTO}) - B_0C_0|^2}, & \mathrm{Re}\left\{D_0 - \frac{B_0C_0}{A_0+k_m}\right\} \geq 0 \\ \frac{2|(A_0+k_m)f_7 - C_0f_3|^2\omega^2 c_{PTO}}{|A_0+k_m|^2\left(\mathrm{Im}\left\{D_0 - \frac{B_0C_0}{A_0+k_m}\right\} + 4\omega c_{PTO}\right)^2}, & \mathrm{Re}\left\{D_0 - \frac{B_0C_0}{A_0+k_m}\right\} < 0. \end{cases} \tag{26}$$

(3) Level I, optimisation of k_m

The expression of the wave power absorption may be written as

$$P = \frac{2|f_7|^2\left|k_m + A_0 - \frac{C_0f_3}{f_7}\right|^2\omega^2 c_{PTO}}{|D_0+4k_{PTO}+4\mathrm{i}\omega c_{PTO}|^2\left|k_m + A_0 - \frac{B_0C_0}{D_0+4k_{PTO}+4\mathrm{i}\omega c_{PTO}}\right|^2}. \tag{27}$$

The corresponding positive k_m that satisfies $\frac{\partial P}{\partial k_m} = 0$ is [29] (see Eq. (28) which is given in Box II) where

$$\zeta_1 + \mathrm{i}\zeta_2 = A_0 - \frac{C_0f_3}{f_7}, \quad \zeta_3 + \mathrm{i}\zeta_4 = A_0 - \frac{B_0C_0}{D_0+4k_{PTO}+4\mathrm{i}\omega c_{PTO}}. \tag{29}$$

However, it should be noticed that the k_m that satisfies $\frac{\partial P}{\partial k_m} = 0$ here results in the minimum of the wave power absorption, rather than the maximum.

The maximum wave power absorption may be achieved as the larger value between the results with $k_m = 0$ or $k_m \to \infty$, i.e.,

$$P^{m}_{max} = max\left\{\frac{2|A_0f_7 - C_0f_3|^2\omega^2 c_{PTO}}{|A_0(D_0+4k_{PTO}+4\mathrm{i}\omega c_{PTO}) - B_0C_0|^2}, \frac{2|f_7|^2\omega^2 c_{PTO}}{|D_0+4k_{PTO}+4\mathrm{i}\omega c_{PTO}|^2}\right\}. \tag{30}$$

This is in line with the research work reported by Phillips [18].

$$k_m = \frac{\zeta_1^2+\zeta_2^2-\zeta_3^2-\zeta_4^2+\sqrt{(\zeta_1^2+\zeta_2^2-\zeta_3^2-\zeta_4^2)^2-4(\zeta_3-\zeta_1)[\zeta_1(\zeta_3^2+\zeta_4^2)-\zeta_3(\zeta_1^2+\zeta_2^2)]}}{2(\zeta_3-\zeta_1)}, \tag{28}$$

Box II.

(4) Level II, optimisation of c_{PTO} and k_{PTO}

P^c_{max} as given in Eq. (22) can be further enlarged with an optimal k_{PTO}. If k_{PTO} and c_{PTO} can be chosen such that:

$$\frac{\partial P}{\partial c_{PTO}} = 0, \quad \frac{\partial P}{\partial k_{PTO}} = 0, \tag{31}$$

for which we have

$$\begin{aligned}&(c_{PTO}, k_{PTO})\\ &=\left(-\frac{\mathrm{Im}\{(A_0+k_m)[(A_0+k_m)^* D_0^* - B_0^* C_0^*]\}}{4|A_0+k_m|^2\omega},\right.\\ &\quad\left.-\frac{\mathrm{Re}\{(A_0+k_m)[(A_0+k_m)^* D_0^* - B_0^* C_0^*]\}}{4|A_0+k_m|^2}\right).\end{aligned} \tag{32}$$

The maximum absorbed wave power under the optimal combination of c_{PTO} and k_{PTO} is

$$P^{c,k}_{max} = -\frac{\omega}{8}\frac{|(A_0+k_m)f_7 - C_0 f_3|^2}{\mathrm{Im}\{(A_0+k_m)[(A_0+k_m)^* D_0^* - B_0^* C_0^*]\}}. \tag{33}$$

If $k_{PTO} < 0$ is obtained with the utilisation of Eq. (32), then c_{PTO}, k_{PTO}, and $P^{c,k}_{max}$ should be recalculated with

$$(c_{PTO}, k_{PTO}) = \left(\frac{|(A_0+k_m)D_0 - B_0 C_0|}{4|A_0+k_m|\omega}, 0\right), \tag{34}$$

and

$$\begin{aligned}P^{c,k}_{max} &= P^c_{max}(k_{PTO}=0)\\ &= \frac{1}{4}\frac{\omega|(A_0+k_m)f_7 - C_0 f_3|^2}{|A_0+k_m||(A_0+k_m)D_0 - B_0 C_0| - \mathrm{Im}\{(A_0+k_m)[(A_0+k_m)^* D_0^* - B_0^* C_0^*]\}}.\end{aligned} \tag{35}$$

(5) Level II, optimisation of c_{PTO} and k_m

The maximum wave power absorption and the corresponding optimised c_{PTO} and k_m can be expressed as

$$\begin{aligned}P^{c,m}_{max} = max\left\{\right.&\frac{1}{4}\frac{\omega|A_0 f_7 - C_0 f_3|^2}{|A_0||A_0(D_0+4k_{PTO}) - B_0 C_0| - \mathrm{Im}\{A_0(A_0^* D_0^* - B_0^* C_0^*)\}},\\ &\left.\frac{1}{4}\frac{\omega|f_7|^2}{|D_0+4k_{PTO}| - \mathrm{Im}\{D_0^*\}}\right\},\end{aligned} \tag{36}$$

and

$$(c_{PTO}, k_m) = \left(\frac{|A_0(D_0+4k_{PTO}) - B_0 C_0|}{4|A_0|\omega}, 0\right) \text{ or } \left(\frac{|D_0+4k_{PTO}|}{4\omega}, \infty\right), \tag{37}$$

depending on which term in the brackets of Eq. (36) is larger.

(6) Level II, optimisation of k_{PTO} and k_m

The maximum wave power absorption and the corresponding optimised k_{PTO} and k_m may be expressed as

$$\begin{aligned}P^{k,m}_{max} = max\left\{\right.&\frac{2|A_0 f_7 - C_0 f_3|^2\omega^2 c_{PTO}}{|A_0|^2\left(\mathrm{Im}\left\{D_0 - \frac{B_0 C_0}{A_0}\right\} + 4\omega c_{PTO}\right)^2},\\ &\left.\frac{2|f_7|^2\omega^2 c_{PTO}}{\left(\mathrm{Im}\{D_0\} + 4\omega c_{PTO}\right)^2}\right\},\end{aligned} \tag{38}$$

and

$$(k_{PTO}, k_m) = \left(-\frac{1}{4}\mathrm{Re}\left\{D_0 - \frac{B_0 C_0}{A_0}\right\}, 0\right) \text{ or } \left(-\frac{1}{4}\mathrm{Re}\{D_0\}, \infty\right), \tag{39}$$

depending on which term in the brackets of Eq. (38) is larger.

If $k_{PTO} < 0$ is obtained with the utilisation of Eq. (39), then k_{PTO}, k_m and $P^{k,m}_{max}$ should be recalculated with

$$\begin{aligned}P^{k,m}_{max} &= P^m_{max}(k_{PTO}=0)\\ &= max\left\{\frac{2|A_0 f_7 - C_0 f_3|^2\omega^2 c_{PTO}}{|A_0(D_0+4i\omega c_{PTO}) - B_0 C_0|^2}, \frac{2|f_7|^2\omega^2 c_{PTO}}{|D_0+4i\omega c_{PTO}|^2}\right\},\end{aligned} \tag{40}$$

and

$$(k_{PTO}, k_m) = (0,0) \text{ or } (0,\infty), \tag{41}$$

depending on which term in the brackets of Eq. (40) is larger.

(7) Level III, optimisation of c_{PTO}, k_{PTO}, and k_m

The maximum wave power absorption and the corresponding optimised c_{PTO}, k_{PTO}, and k_m may be expressed as

$$P_{MAX} = max\left\{-\frac{\omega}{8}\frac{|A_0 f_7 - C_0 f_3|^2}{\mathrm{Im}\{A_0(A_0^* D_0^* - B_0^* C_0^*)\}}, -\frac{\omega}{8}\frac{|f_7|^2}{\mathrm{Im}\{D_0^*\}}\right\}, \tag{42}$$

and

$$\begin{aligned}&(c_{PTO}, k_{PTO}, k_m)\\ &=\left(-\frac{\mathrm{Im}\{A_0(A_0^* D_0^* - B_0^* C_0^*)\}}{4|A_0|^2\omega}, -\frac{\mathrm{Re}\{A_0(A_0^* D_0^* - B_0^* C_0^*)\}}{4|A_0|^2}, 0\right) \text{ or}\\ &\left(-\frac{\mathrm{Im}\{D_0^*\}}{4\omega}, -\frac{1}{4}\mathrm{Re}\{D_0^*\}, \infty\right),\end{aligned} \tag{43}$$

depending on which term in the brackets of Eq. (42) is larger.

It is noted that when the stiffness of the mooring system $k_m \to \infty$, this equation becomes $P_{MAX} = \frac{|f_7|^2}{8c_{7,7}}$, which coincides with the maximum absorbed power that a Clam-motion only C-WEC, i.e., no motion in the heave mode, can achieve in resonant conditions as expected.

Again, if the value of k_{PTO} evaluated with the employment of Eq. (43) is negative, c_{PTO}, k_{PTO}, k_m and P_{MAX} should be recalculated by

$$\begin{aligned}P_{MAX} &= P^{c,m}_{max}(k_{PTO}=0)\\ &= max\left\{\frac{1}{4}\frac{\omega|A_0 f_7 - C_0 f_3|^2}{|A_0||A_0 D_0 - B_0 C_0| - \mathrm{Im}\{A_0(A_0^* D_0^* - B_0^* C_0^*)\}},\right.\\ &\quad\left.\frac{1}{4}\frac{\omega|f_7|^2}{|D_0| - \mathrm{Im}\{D_0^*\}}\right\},\end{aligned} \tag{44}$$

and

$$(c_{PTO}, k_{PTO}, k_m) = \left(\frac{|A_0 D_0 - B_0 C_0|}{4|A_0|\omega}, 0, 0\right) \text{ or } \left(\frac{|D_0|}{4\omega}, 0, \infty\right), \tag{45}$$

depending on which term in the brackets of Eq. (44) is larger.

4. Results and discussions

The geometry of the C-WEC considered hereinafter and the corresponding mesh arrangements of the wetted surface are presented in Fig. 3. The uprights connecting the keel to the wedge are thin and have little impact on hydrodynamics. Hence they are omitted in the hydrodynamic simulation. Following Phillips [18]'s work, the hinge point

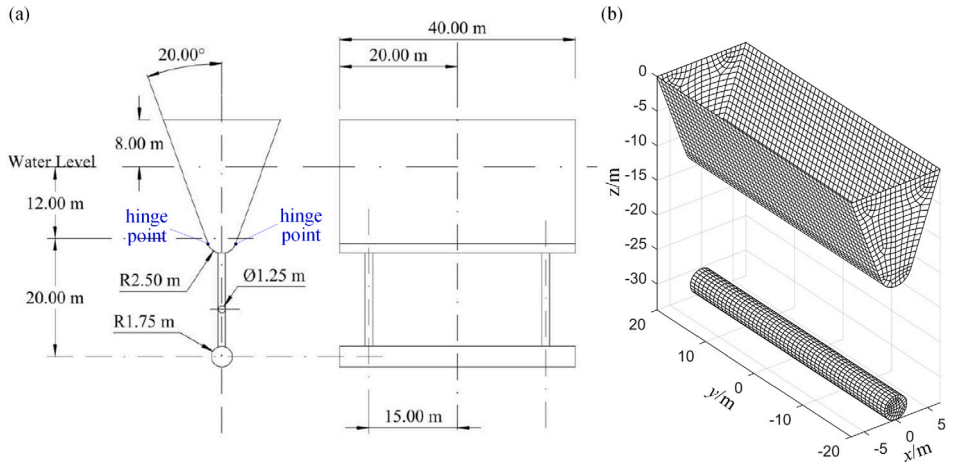

Fig. 3. (a) Model geometry of the C-WEC [18]; (b) Mesh arrangements of the C-WEC.

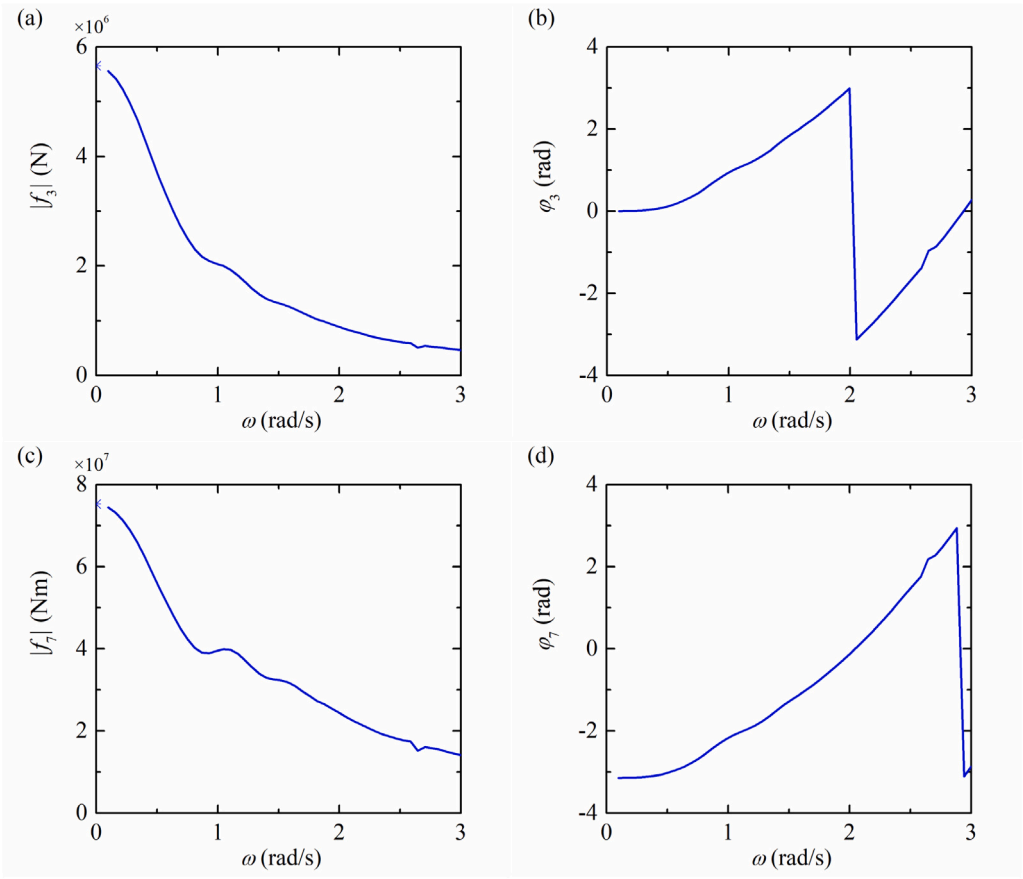

Fig. 4. Frequency response of the wave excitation force/moment acting on the C-WEC: (a) amplitude of the heave excitation force, $|f_3|$; (b) phase of the heave excitation force, φ_3; (c) amplitude of the Clam excitation moment, $|f_7|$; (d) phase of the Clam excitation moment, φ_7.

positions for the right-hand side flap and the left-hand side one are $(x_{0+}, z_0) = (2.348\text{ m}, -12.854\text{ m})$ and $(x_{0-}, z_0) = (-2.348\text{ m}, -12.854\text{ m})$, respectively (i.e., $d = 12.854$ m). Water depth is $h = 100$ m unless otherwise specified. $m = 5.561 \times 10^6$ kg, $m_0 = 0$, $I = 0$, $k_{3,3} = 5.6535 \times 10^6$ N/m. The mass is symmetrically distributed about $x = 0$ and $y = 0$ planes, hence the centre of gravity of the device is located on the z-axis.

The PTO damping, PTO stiffness, and mooring stiffness may be nondimensionalised into

$$\bar{c}_{PTO} = \frac{c_{PTO}\sqrt{gh}}{\rho g b d^4}; \quad \bar{k}_{PTO} = \frac{k_{PTO}}{\rho g b d^3}; \quad \bar{k}_m = \frac{k_m}{\rho g S}. \tag{46}$$

Figs. 4 and 5 present the frequency response of the wave excitation forces and the hydrodynamic coefficients evaluated by WAMIT. As expected, $m_{7,3} = m_{3,7}$ and $c_{7,3} = c_{3,7}$ are satisfied by the numerical results. To shorten the length of the paper, $m_{7,3}$ and $c_{7,3}$ are not plotted in Fig. 5.

4.1. Model validation

Fig. 6 shows a comparison between the present numerical results of the heave RAO and Clam RAO of the device and the corresponding

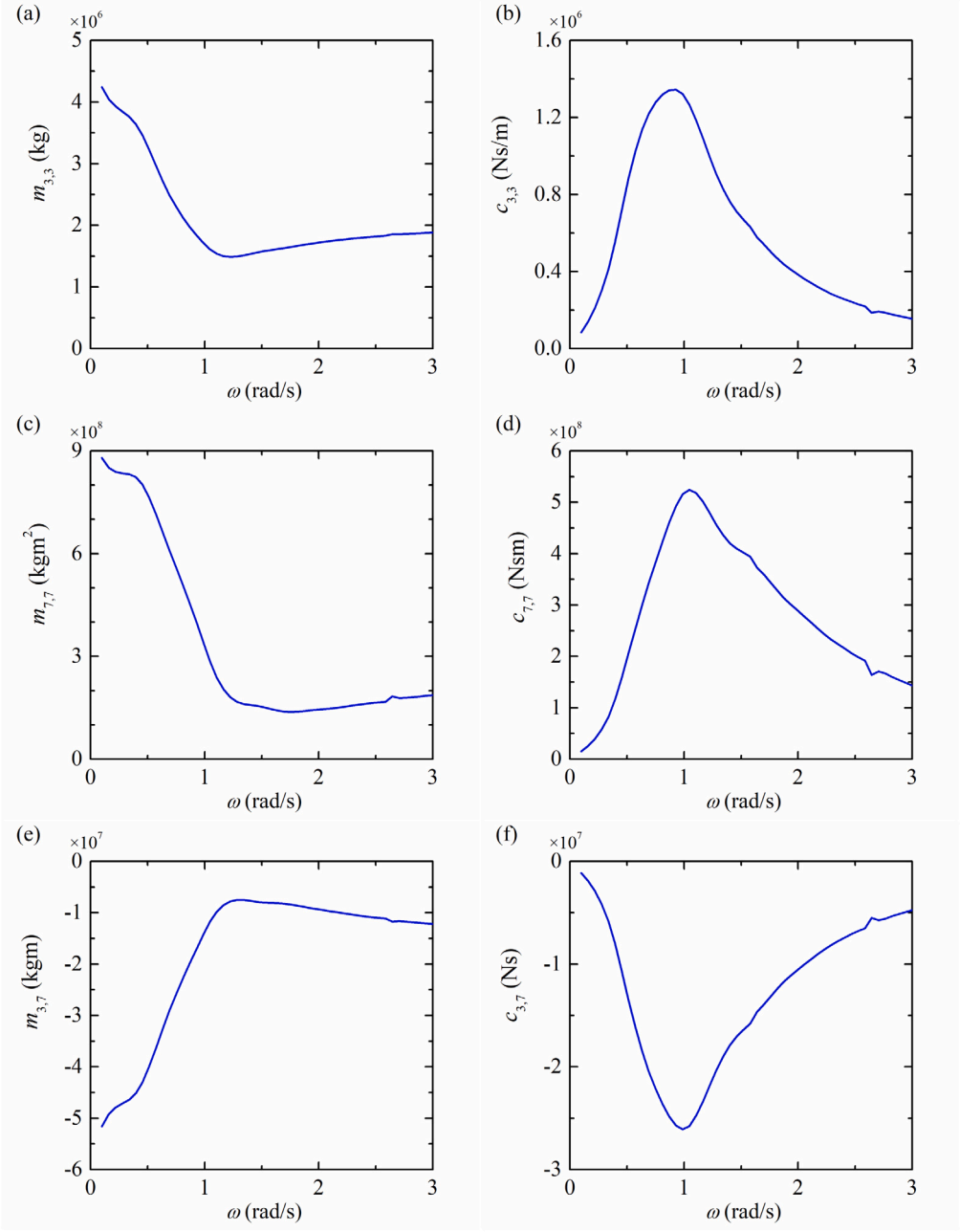

Fig. 5. Frequency response of the hydrodynamic coefficients of the C-WEC (a) $m_{3,3}$; (b) $c_{3,3}$; (c) $m_{7,7}$; (d) $c_{7,7}$; (e) $m_{3,7}$; (f) $c_{3,7}$.

measured physical data, which has been scaled up to the full prototype from the 1:50 experimental model. The 1:50 scale physical tests were carried out in the Ocean Basin at the Coastal, Ocean and Sediment Transport (COAST) laboratory, housed in the Marine Building at the University of Plymouth [18]. The numerical predictions are generally in good agreement with the experiment data, although there are some discrepancies between $T = 9$ and 14 s. Fig. 7 presents the frequency response of η_{max}^{c} and c_{opt} obtained by using the present analytical model. For comparison, the results predicted with the employment of the trial and error method (i.e., an exhaustive search method), which finds the optimisation solution by trying a finite number of attempts over a specified range of the value of a variable (e.g., the PTO damping coefficient) and then comparatively evaluating the solutions based upon some predefined set of criteria (e.g., the maximum wave power absorption), are also displayed. A good agreement of the present results with the trial and error numerical results is achieved, and it gives us confidence in the present model for solving wave diffraction/radiation problems and evaluating the maximum wave power absorption of the C-WEC.

Hereinafter, the validated model is adopted to predict the potential maximum wave power absorption of the device and evaluate the corresponding optimised PTO system or/and mooring stiffness.

4.2. Optimisation of the PTO damping coefficient

Fig. 8 illustrates the frequency response of $\eta_{max}^{(c)}$ and $\bar{c}_{opt}^{(c)}$ of the C-WEC with $\bar{k}_m = 0$, i.e., the device is free-floating. Different curves denote the device with different values of PTO stiffness ($\bar{k}_{PTO}$). For 1 rad/s < ω < 2 rad/s, in the examined five cases, the larger $\bar{k}_{PTO}$, the smaller $\eta_{max}^{(c)}$ and the larger the corresponding $\bar{c}_{opt}^{(c)}$. At $\omega \approx 0.87$ rad/s, the change in $\bar{k}_{PTO}$ has little impact on $\eta_{max}^{(c)}$ and $\bar{c}_{opt}^{(c)}$. This is because $|A_0|$ is rather small at $\omega \approx 0.87$ rad/s, making $\eta_{max}^{(c)}$ and $\bar{c}_{opt}^{(c)}$ insensitive

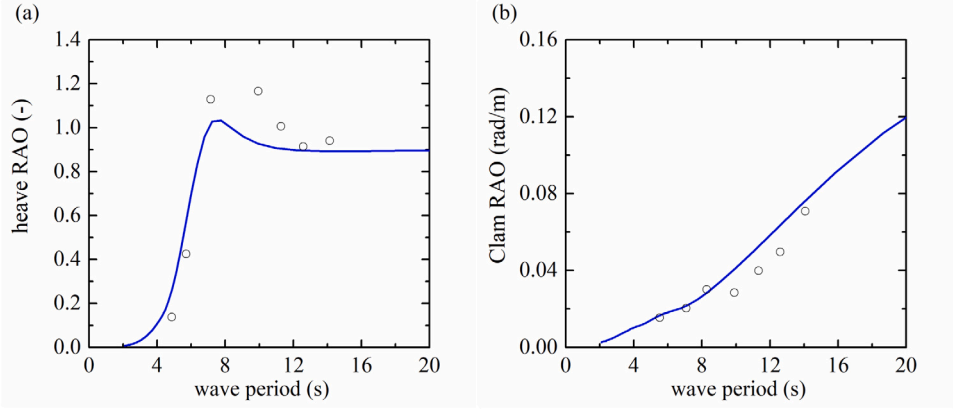

Fig. 6. Comparison between the numerical results and the physical data (a) heave RAO $|\xi_3|/A$ of a floating C-WEC with fixed Clam angle for $c_h = 10^6$ Ns/m, $k_m = 6 \times 10^5$ N/m; (b) Clam RAO $|\xi_7|/A$ of a C-WEC fixed in heave for $c_{PTO} = 3.9 \times 10^8$ N m s/rad and $k_{PTO} = 1.6 \times 10^7$ N m/rad. lines: numerical results; symbols: measured physical data [18].

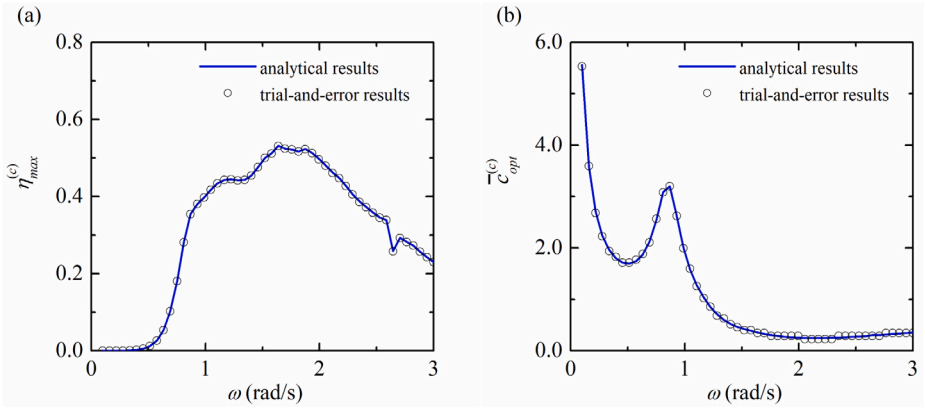

Fig. 7. Frequency response of the maximum wave power absorption efficiency and the corresponding optimised PTO damping with $k_{PTO} = 0$ and $k_m = 0$, level I, optimisation of c_{PTO}: (a) $\eta_{max}^{(c)}$; (b) $c_{opt}^{(c)}$.

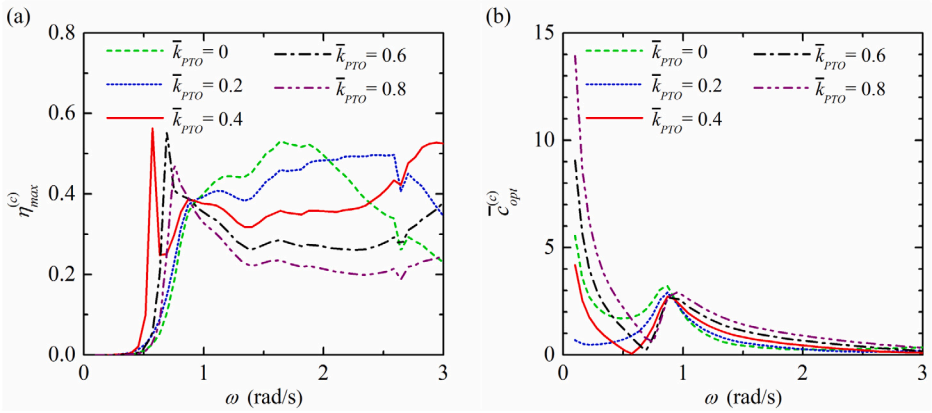

Fig. 8. Variation of $\eta_{max}^{(c)}$ and $\bar{c}_{opt}^{(c)}$ with ω for different $\bar{k}_{PTO}$ and $\bar{k}_m = 0$.

to the change of $\bar{k}_{PTO}$ (see Eqs. (21) and (22)). For $\bar{k}_{PTO} \geq 0.4$, a local peak of $\eta_{max}^{(c)}$ occurs at $\omega < 1.0$ rad/s, where a local minimum of $\bar{c}_{opt}^{(c)}$ is observed. This is because $D_0 - B_0 C_0 / A_0 \approx \mathbb{R}^-$ for $\omega < 1.0$ rad/s. When $\bar{k}_{PTO}$ is large enough, say $\bar{k}_{PTO} \geq 0.4$, $|D_0 + 4k_{PTO} - B_0 C_0 / A_0| \approx 0$ can be achieved (see Eqs. (21) and (22)), leading to a local peak and valley of the frequency responses of $\eta_{max}^{(c)}$ and $\bar{c}_{opt}^{(c)}$, respectively. When the incident wavelength is large, say $\omega < 0.5$ rad/s, the free-floating device moves up and down with the waves and the Clam-mode motion can be hardly excited to capture wave power.

We select $\omega = 0.5$, 1.0, 1.5, 2.0, and 2.5 rad/s as five typical wave conditions and plot the corresponding $\eta_{max}^{(c)} - \bar{k}_{PTO}$ and $\bar{c}_{opt}^{(c)} - \bar{k}_{PTO}$ in Fig. 9. For intermediate wave frequencies in the examined five wave conditions, $\omega = 1.0$ and 1.5 rad/s, the largest value of $\eta_{max}^{(c)}$ is achieved without a PTO stiffness. Whereas for the remaining low and high wave frequencies (i.e., $\omega = 0.5$, 2.0, and 2.5 rad/s), there is an optimised non-vanishing $\bar{k}_{PTO}$ to maximise $\eta_{max}^{(c)}$. For any specified wave condition, the variation of $\bar{c}_{opt}^{(c)}$ with $\bar{k}_{PTO}$ shows an opposite trend to that of the $\eta_{max}^{(c)} - \bar{k}_{PTO}$. For the lowest wave frequency, $\omega = 0.5$ rad/s, a sharp peak

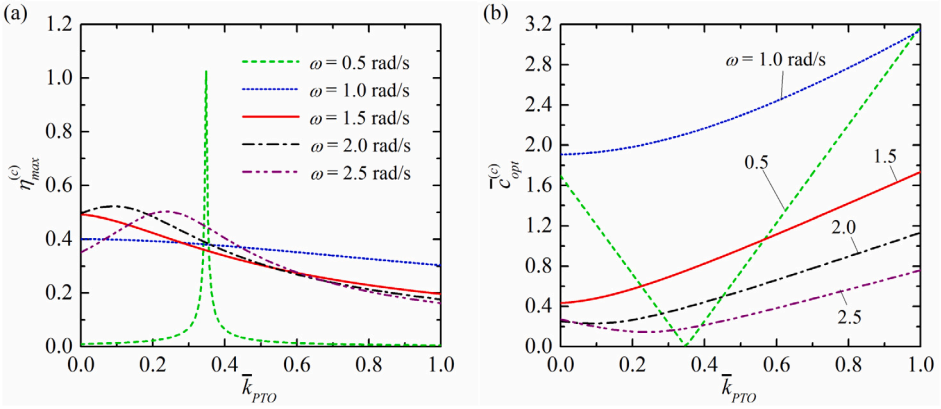

Fig. 9. Variation of $\eta^{(c)}_{max}$ and $\bar{c}^{(c)}_{opt}$ with $\bar{k}_{PTO}$ for different ω and $\bar{k}_m = 0$.

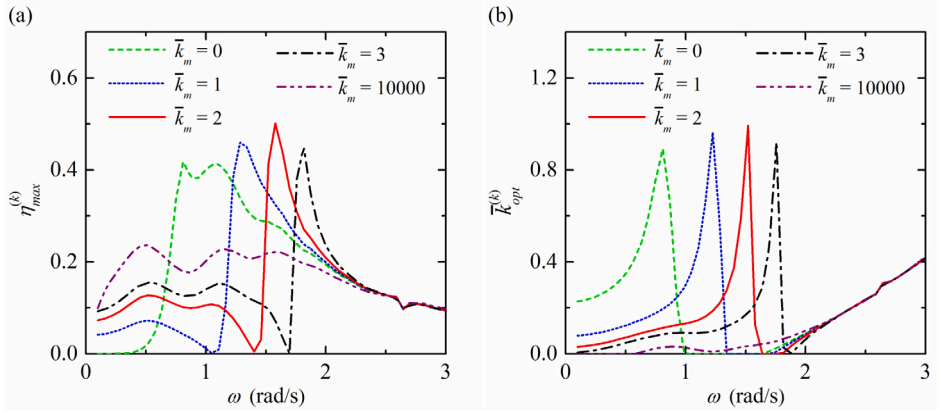

Fig. 10. Variation of $\eta^{(k)}_{max}$ and $\bar{k}^{(k)}_{opt}$ with ω for different $\bar{k}_m$ and $\bar{c}_{PTO} = 2.0$.

of $\eta^{(c)}_{max} - \bar{k}_{PTO}$ and a relatively linear $\bar{c}^{(c)}_{opt} - \bar{k}_{PTO}$ are observed. This is because when $\omega \to 0$, wave radiation damping coefficients $\to 0$, and A_0, B_0, C_0, and D_0 all tend to be real numbers. Hence Eqs. (21) and (22) tend to be the amplitudes of a linear function and a reciprocal function of k_{PTO}, respectively, leading to the results for small wave frequencies, e.g., $\omega = 0.5$ rad/s, as plotted in Fig. 9.

4.3. Optimisation of the PTO stiffness coefficient

Fig. 10 displays the frequency response of $\eta^{(k)}_{max}$ and $\bar{k}^{(k)}_{opt}$ of the C-WEC with a specified PTO damping, $\bar{c}_{PTO} = 2.0$. Different curves represent the device by applying the mooring system with different stiffness. When the device is free-floating, i.e., $\bar{k}_m = 0$, very little wave power can be captured by the device for $\omega < 0.5$ rad/s. As ω increases from 0.5 rad/s, $\eta^{(k)}_{max}$ shows a rapid increase and reaches the maximum value 0.4 around $\omega = 1$ rad/s. As ω keeps increasing, $\eta^{(k)}_{max}$ starts decreasing. As $\bar{k}_m$ increases from 0 to 3, the main peak of $\eta^{(k)}_{max} - \omega$ curve shifts towards large wave frequencies and the bandwidth becomes smaller and smaller. Meanwhile, the curve for small wave frequencies, e.g., $\omega < 0.5$ rad/s, raises up with the increase of $\bar{k}_m$. It is noted that for mooring stiffness $\bar{k}_m = 1$, 2, and 3, no wave power can be captured at $\omega = 1.1$, 1.4, and 1.7 rad/s, respectively. This is because $A_0 - C_0 f_3 / f_7 \approx \mathbb{R}^-$, and we have $|k_m + A_0 - C_0 f_3 / f_7| \approx 0$ at specific wave conditions for these three cases, resulting in no wave power absorption regardless of the values of the PTO damping and stiffness (see Eq. (20)). When the wave frequencies become large enough, e.g., $\omega > 2.3$ rad/s, $\eta^{(c)}_{max}$ and $\bar{k}^{(k)}_{opt}$ are found to be insensitive to the change of $\bar{k}_m$.

4.4. Optimisation of the mooring stiffness coefficient

Fig. 11 exhibits the frequency response of $\eta^{(m)}_{max}$ and $\bar{k}^{(m)}_{m,opt}$, and different curves represent the cases with different PTO damping. In long waves, e.g., $\omega < 0.7$ rad/s, the maximum wave power absorption of the device is achieved when the mooring stiffness is infinite, i.e., the heave motion of the device is completely restricted (see Fig. 11b). Whereas for 1.0 rad/s $< \omega <$ 2.5 rad/s, the free-floating device without any constraint from the mooring system can capture more wave power than those with some mooring restraints. In the examined five cases, the smaller the PTO damping, the larger $\eta^{(m)}_{max}$ is obtained for most wave conditions, except ω around 1.0 rad/s.

4.5. Optimisation of both PTO damping coefficient and PTO stiffness coefficient

Fig. 12 shows the maximum wave power absorption of the C-WEC when the PTO damping and PTO stiffness are both optimised. Different curves denote the cases with different values of mooring stiffness. For long-wave conditions, e.g., $\omega < 0.5$ rad/s, the longer the incident waves, the larger the maximum wave power capture factor, except the two cases with $\bar{k}_m = 4$ and 10 000, for which $\bar{k}^{(ck)}_{opt} = 0$, and $\partial P / \partial k_{PTO} = 0$ is not satisfied, meaning the resonance condition is not achieved. For $\omega >$ 0.5 rad/s, the $\eta^{(ck)}_{max} - \omega$ curves for the examined six cases almost overlap one another, except three steps observed at 1.1, 1.4, and 1.7 rad/s for $\bar{k}_m = 1$, 2, and 3, respectively, where we have $|k_m + A_0 - C_0 f_3 / f_7| \approx 0$ as reported in Section 4.3. Fig. 12a exhibits that $\eta^{(ck)}_{max} \approx 0.5$ for $\omega >$ 2.0 rad/s. This may be explained from the two-dimensional point of

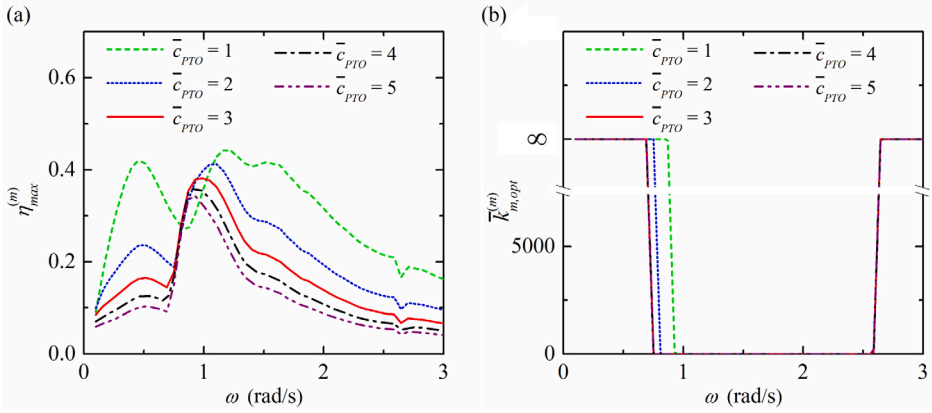

Fig. 11. Variation of $\eta_{max}^{(m)}$ and $\bar{k}_{m,opt}^{(m)}$ with ω for different $\bar{c}_{PTO}$ and $\bar{k}_{PTO}=0$.

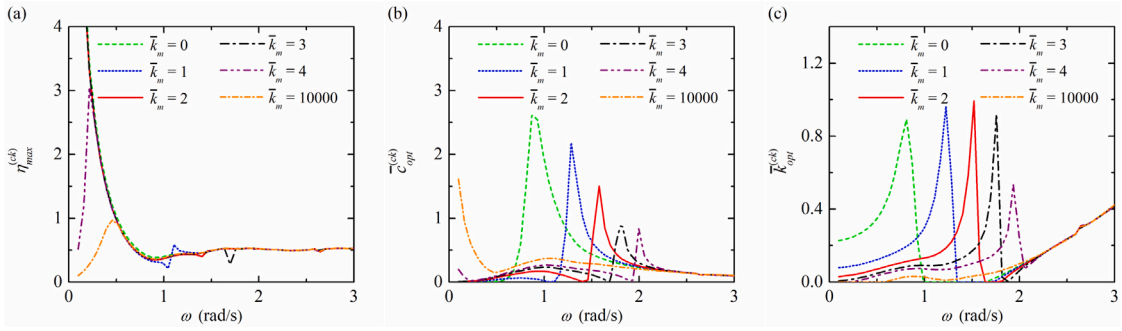

Fig. 12. Variation of $\eta_{max}^{(ck)}$, $\bar{c}_{opt}^{(ck)}$ and $\bar{k}_{opt}^{(ck)}$ with ω for different $\bar{k}_m$.

view: when the incident wavelength is much smaller than the width of the device, the hydrodynamic problem becomes a two-dimensional case. In the two-dimensional case, because the device is symmetric so that waves are radiated from the device equally in opposite directions, meaning that not more than 50% of the incident wave energy can be captured.

4.6. Optimisation of PTO damping coefficient, PTO stiffness coefficient and mooring stiffness coefficient

Fig. 13 illustrates the frequency response of the maximum wave power capture factor of the device when the PTO damping, PTO stiffness, and the mooring stiffness are all optimised. As ω increases from 0.1 rad/s, $\eta_{max}^{(ckm)}$ exhibits a rapid decrease first and reaches the minimum around $\omega = 0.9$ rad/s. As ω keeps increasing, $\eta_{max}^{(ckm)}$ increases slightly and remains at 0.5 when $\omega > 1.6$ rad/s. $\eta_{max}^{(ckm)} > 1.0$ is obtained for $\omega < 0.5$ rad/s, and it should be pointed out that the corresponding $\bar{c}_{opt}^{(ckm)}$ is rather small, meaning that a large response in the Clam-mode is required. This, however, may not be achievable in practical applications since the C-WEC would have physical limitations placed upon excursions due to restraints such as pump stroke, and what is more, the present linear theory may not be valid when the device response is too severe.

4.7. Effect of the width

Wave energy could increase the power generated and reduce the LCoE (Levelised cost of energy) by increasing the device scale [30]. In the above subsections, it shows that the maximum wave power capture factor around $\omega = 1.0$ rad/s can be achieved with $\bar{c}_{PTO} = 2.0$, $\bar{k}_{PTO} = 0$ and $\bar{k}_m = 0$. In this subsection, we keep adopting these settings and examine the performance of the device with different width, $\bar{b} = 0.2$, 0.3, 0.4, 0.5, and 0.6. The frequency response of the wave power capture factor η is displayed in Fig. 14. The effect of device width on wave power absorption mainly happens at 0.8 rad/s $< \omega <$ 1.7 rad/s. For $\bar{b} < 0.4$, there are two peaks of η observed in this range of wave conditions, and as $\bar{b}$ keeps increasing towards 0.6, these two peaks merge into one single peak with the peak value increasing and approaching 0.5.

Fig. 15 plots the maximum wave power absorption when the PTO damping can be optimised. It shows that the smaller width of the C-WEC, the larger the range of $\bar{c}_{opt}^{(c)}$ is required around $\omega = 1.0$ rad/s, making it more difficult to control in practice.

The maximum wave power absorption of a free-floating C-WEC when the PTO damping and PTO stiffness can be both optimised is displayed in Fig. 16. The smaller the width of the device, the larger $\eta_{max}^{(ck)}$ is exhibited for $\omega < 0.8$ rad/s. This is because when the device width gets small, the device acts as a point absorber. The point absorber effect (also known as the antenna effect), which is the ability to absorb power from a larger width than the physical dimension of the device, becomes stronger with the decrease of the device width. Whereas in short waves, e.g., $\omega > 2.0$ rad/s, the performance of the C-WEC in terms of wave power capture factor remains 0.5 for the examined five cases with different width. As ω decreases from 1.0 rad/s to 0.1 rad/s, $\eta_{max}^{(ck)}$ shows a more and more rapid increase. For $\omega < 0.5$ rad/s, the narrower the device, the higher the $\eta_{max}^{(ck)}$. When ω is small enough, $\eta_{max}^{(ck)} > 5$ can be achieved for all the examined five cases. However, this may not be achievable in practical applications. To achieve such a high $\eta_{max}^{(ck)}$, a rather large device motion is required, and it could make the assumptions of linear theory invalid. Moreover, there are physical limitations to restricting the motion amplitude, e.g., pump stroke and mooring lines. It would be better to consider the effect of a constraint on the performance of the device. Similar studies were reported in the context of point absorbers (e.g., see [31]) and two-hinged-raft devices

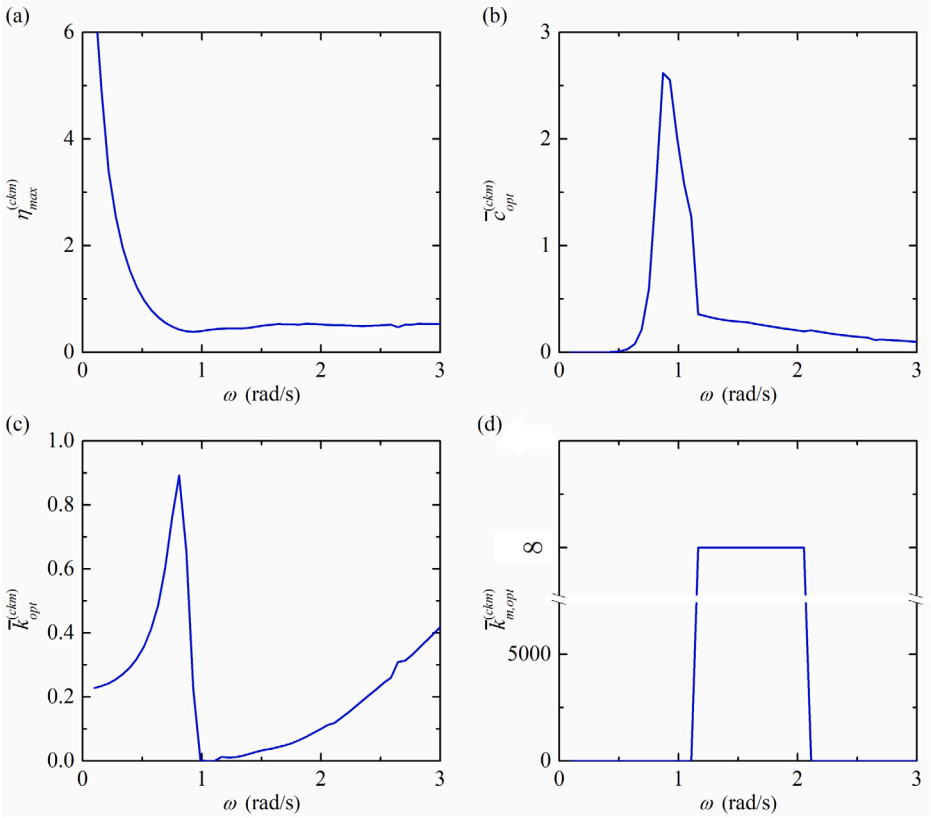

Fig. 13. Variation of $\eta_{max}^{(ckm)}$, $\bar{c}_{opt}^{(ckm)}$, $\bar{k}_{opt}^{(ckm)}$ and $\bar{k}_{m,opt}^{(ckm)}$ with ω.

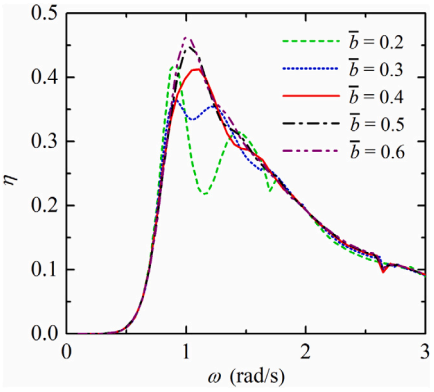

Fig. 14. Variation of η with ω for the devices with different width, $\bar{c}_{PTO} = 2.0$, $\bar{k}_{PTO} = 0$ and $\bar{k}_m = 0$.

(e.g., see [32]). This evaluation is beyond the scope of this paper and, therefore, is left for future work. It should also be pointed out that the absorbed wave power is expressed in terms of wave energy capture width ratio (see Eq. (18)), meaning that plenty of wave power could be captured by the device with a large width even if the wave energy capture width ratio is low.

4.8. Effect of the opening angle

The opening angle of the device in still water in terms of 2θ can be adjusted by changing the initial PTO moment (M_0) acting on the flap in still water. Note that the submergence of the clam (d) at the equilibrium would also change accordingly with the change of θ should other parameters be fixed.

Fig. 17 presents the variation of d of the device with θ in still water for the free-floating cases with $F_{m,0} = 0$. The weight of the device does not change, meaning the displacement volume is fixed, hence the submergence of the device decreases with the increase of the opening angle as expected. $\theta = 20°$, $25°$, $30°$, $35°$, $40°$, $45°$, $50°$ correspond to $d = 12.854$ m, 11.810 m, 10.941 m, 10.187 m, 9.508 m, 8.878 m, and 8.276 m, respectively. Fig. 18 presents the frequency responses of $\eta_{max}^{(ck)}$ and the optimised PTO damping and stiffness in terms of $\bar{c}_{opt}^{(ck)*} = c_{opt}^{(ck)}\sqrt{g/h}/(\rho g b d_0^4)$ and $\bar{k}_{opt}^{(ck)*} = k_{opt}^{(ck)}/(\rho g b d_0^3)$, respectively, for the device with different opening angles in still water, where $d_0 = 12.854$ m. For $\omega < 1.0$ rad/s, the $\eta_{max}^{(ck)} - \omega$ curves for the examined seven cases overlap with one other, demonstrating the independence of $\eta_{max}^{(ck)}$ on the opening angle of the device. Whereas for $\omega \approx 2.0$ rad/s, as θ increases from 20° to 50°, less and less wave power can be captured by the device. This may be because the larger the opening angle, the smaller the submerged depth, and the smaller both the hydrodynamic force acting on the flaps and the moment arm about the hinges, leading to smaller hydrodynamic moments about the hinges and resulting in a worse performance of the device in wave power absorption. A main peak of the $\bar{c}_{opt}^{(ck)*} - \omega$ curve is observed around $\omega = 1.0$ rad/s regardless of the values of the device opening angle in still water. The peak value of $\bar{c}_{opt}^{(ck)*}$ is found to be strongly dependent on the value of θ, and the larger the opening angle, the smaller the peak value. This makes sense because when the optimum phase condition and optimum amplitude condition are satisfied simultaneously we have $\bar{c}_{opt}^{(ck)*} \approx c_{7,7}$ [33], in which $c_{7,7}$ becomes smaller when the opening angle of the device is increased, i.e., the submerged depth is decreased, in still water.

To achieve the maximum wave power absorption as plotted in Fig. 18a, both PTO damping and PTO stiffness need to be adapted, and

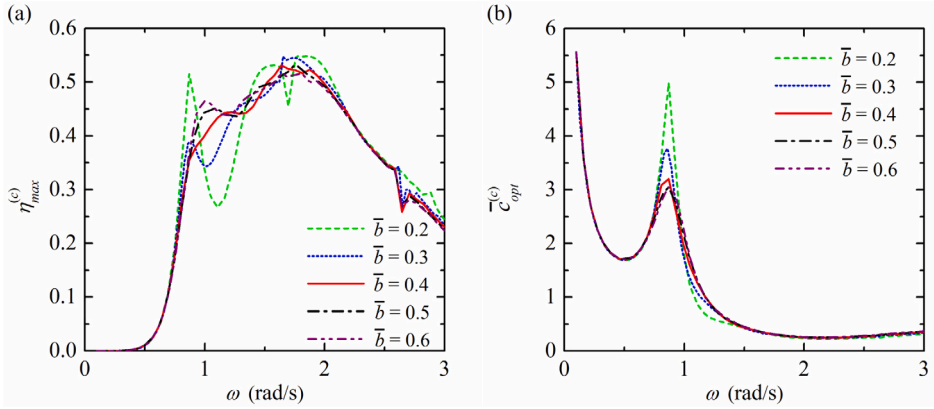

Fig. 15. Variation of $\eta_{max}^{(c)}$ and $\bar{c}_{opt}^{(c)}$ with ω for the devices with different width, $\bar{k}_{PTO} = 0$ and $\bar{k}_m = 0$.

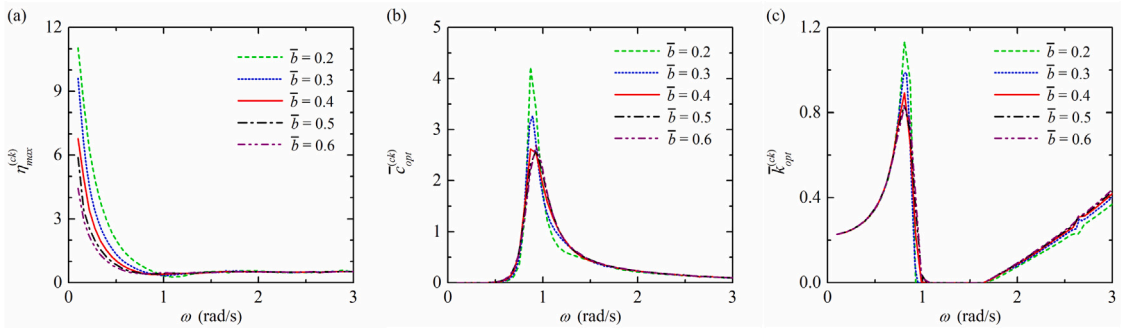

Fig. 16. Variation of $\eta_{max}^{(ck)}$, $\bar{c}_{opt}^{(ck)}$ and $\bar{k}_{opt}^{(ck)}$ with ω for the devices with different width and $\bar{k}_m = 0$.

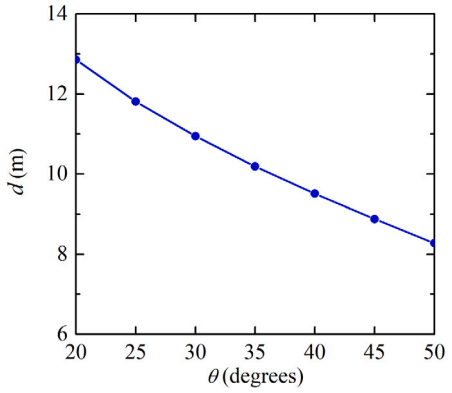

Fig. 17. Variation of the submerged depth of the flaps (d) with θ (the opening angle between the two flaps is 2θ) in still water.

a large variation range of wave frequency dependent $\bar{c}_{opt}^{(ck)*}$ and $\bar{k}_{opt}^{(ck)*}$ could be required over the examined wave conditions, especially for $\theta = 20°$ (see Figs. 18b and c). This may increase the system complexity and costs of the device. For simplicity, choosing a proper PTO stiffness and optimising only the PTO damping to improve the power capture ability of the device may be welcomed. Fig. 19 presents the frequency response of $\eta_{max}^{(c)}$ and $\bar{c}_{opt}^{(c)*}$ for seven different opening angles with $\bar{k}_{PTO}^{*} = 0.3$ and $\bar{k}_m = 0$. In the examined seven cases, a spike of the $\eta_{max}^{(c)} - \omega$ curve and a valley of the $\bar{c}_{opt}^{(c)*} - \omega$ curve are observed, respectively, between $\omega = 0.4$ rad/s and 0.8 rad/s. This is because A_0, B_0, C_0, and D_0 all tend to be real numbers as wave radiation damping $\to 0$ when $\omega \to 0$, and meanwhile, $A_0(D_0 + 4k_{PTO} - B_0C_0) \approx 0$ is satisfied for a specified wave frequency between $\omega = 0.4$ rad/s and 0.8 rad/s for the examined seven cases. $A_0(D_0 + 4k_{PTO} - B_0C_0) \approx 0$ is located at the denominator and numerator in the expressions of the maximum absorbed wave power and optimised PTO damping, respectively (see Eqs. (21) and (22)), resulting in a local peak of the $\eta_{max}^{(c)} - \omega$ curve and a local valley of the $\bar{c}_{opt}^{(c)*} - \omega$ curve between $\omega = 0.4$ rad/s and 0.8 rad/s. The larger the θ, the larger the heaving stiffness ($k_{3,3}$) and the clam stiffness ($k_{7,7}$), making the local peak of the $\eta_{max}^{(c)} - \omega$ curve and the local valley of the $\bar{c}_{opt}^{(c)*} - \omega$ curve move towards large wave frequencies.

5. Conclusions

In this paper, a Clam-type wave energy converter (C-WEC), which consists of a pair of flaps that are hinged at the bottom, is considered. The relative rotation of the flaps, i.e., the so-called Clam-motion, is utilised to capture energy from water waves. To investigate the performance of the C-WEC, a numerical model based on the linear potential flow theory is developed. What is more, the maximum wave power that can be captured by the device when the PTO/mooring system can be optimised is predicted. Some selected findings are listed below.

- When the incident wavelength is large, the Clam-mode motion of the free-floating device without any mooring restraints is hardly excited to capture wave power.
- For some specific mooring stiffness, no wave power could be captured by the device for particular wave conditions regardless of the values of the PTO damping and stiffness.
- When the PTO stiffness and mooring stiffness of the device are both variable, their optimised values are found to be independent of the PTO damping.
- For the freely floating C-WEC with $\bar{c}_{PTO} = 2.0$ and $\bar{k}_{PTO} = 0$, there are two peaks of the frequency response of wave power capture factor when the device width is small, e.g., $\bar{b} < 0.4$. Whereas when

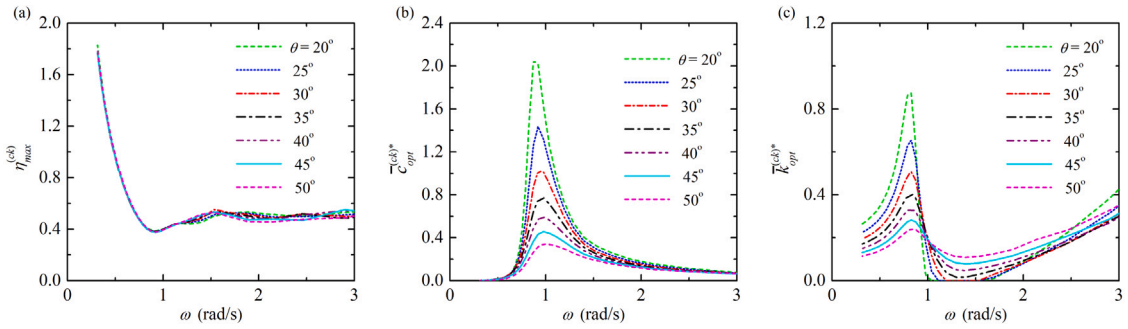

Fig. 18. Variation of $\eta_{max}^{(ck)}$, $\bar{c}_{opt}^{(ck)*}$ and $\bar{k}_{opt}^{(ck)*}$ with ω for different values of θ (the opening angle between the two flaps is 2θ) in still water, $\bar{k}_m = 0$, and $h = 60$ m.

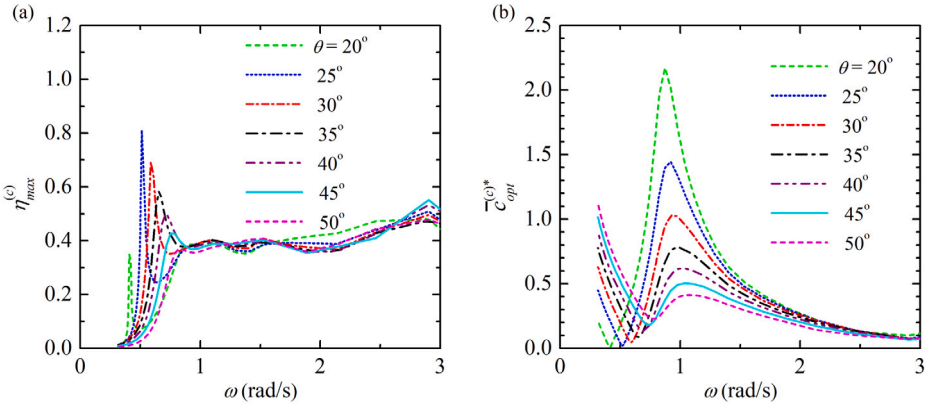

Fig. 19. Variation of $\eta_{max}^{(c)}$ and $\bar{c}_{opt}^{(c)*}$ with ω for different values of θ (the opening angle between the two flaps is 2θ) in still water, $\bar{k}_m = 0$, $\bar{k}_{PTO}^* = 0.3$, and $h = 60$ m.

the device width is large, there is only one single peak, and the peak value becomes larger with the increase of the device width.

- A spike of the frequency response of the maximum wave power capture factor for a free-floating device with a constant PTO stiffness and an optimised PTO damping is observed. The spike moves towards large wave frequencies when the opening angle of the device in still water gets larger.

The present model is developed in the framework of potential flow theory, hence it may not be suitable for the extreme wave–structure interactions. A fully nonlinear hydrodynamic numerical model will be developed in the near future to predict the performance of C-WEC in extreme wave conditions and study the nonlinear characteristics of the mooring system and complex PTO system.

CRediT authorship contribution statement

Siming Zheng: Conceptualization, Methodology, Software, Formal analysis, Validation, Visualization, Writing – original draft, Writing – review & editing. **John Wilfrid Phillips:** Conceptualization, Methodology, Investigation, Writing – review & editing. **Martyn Hann:** Conceptualization, Methodology, Writing – review & editing. **Deborah Greaves:** Conceptualization, Methodology, Writing – review & editing, Funding.

Declaration of competing interest

The authors declare that they have no known competing financial interests or personal relationships that could have appeared to influence the work reported in this paper.

Acknowledgements

The research was supported by the EPSRC, United Kingdom project EP/V040367/1–"Flexible Responsive Systems in Wave Energy: FlexWave". S.Z. acknowledges the EPSRC for supporting part of this work through the PRIMaRE Early Career Researcher Small Research Project (ECR-SRP), United Kingdom. S.Z. wishes to thank Prof. Rod Rainey from the University of Southampton for valuable discussions. D.G. gratefully acknowledges the EPSRC for supporting part of this work through the Supergen ORE Hub, United Kingdom, EP/S000747/1.

Appendix. Derivation of the expressions of K_s and M

Expressions of $k_{3,3}$ and $k_{3,7}$ can be obtained by taking the partial derivatives of the left-hand side of Eq. (1) with respect to d and $-\theta$, respectively,

$$k_{3,3} = \partial\left[\rho g b d^2 \tan\theta + F_s - (2m_0 + m_s)g\right]/\partial d = 2\rho g b d \tan\theta, \tag{A.1}$$

$$k_{3,7} = -\partial\left[\rho g b d^2 \tan\theta + F_s - (2m_0 + m_s)g\right]/\partial\theta = -\frac{\rho g b d^2}{\cos^2\theta}. \tag{A.2}$$

Similarly, $k_{7,3}$ and $k_{7,7}$ can be obtained by taking the partial derivatives of the left-hand side of Eq. (2) with respect to d and $-\theta$, respectively,

$$k_{7,3} \approx \partial\left[2M_s + m_0\ gl\sin\theta - \frac{\rho g b d^3}{3\cos^2\theta}\right]/\partial d = -\frac{\rho g b d^2}{\cos^2\theta}, \tag{A.3}$$

$$k_{7,7} \approx -\partial\left[2M_s + m_0\ gl\sin\theta - \frac{\rho g b d^3}{3\cos^2\theta}\right]/\partial\theta = \frac{2\rho g b d^3\tan\theta}{3\cos^2\theta} - m_0\ gl\cos\theta. \tag{A.4}$$

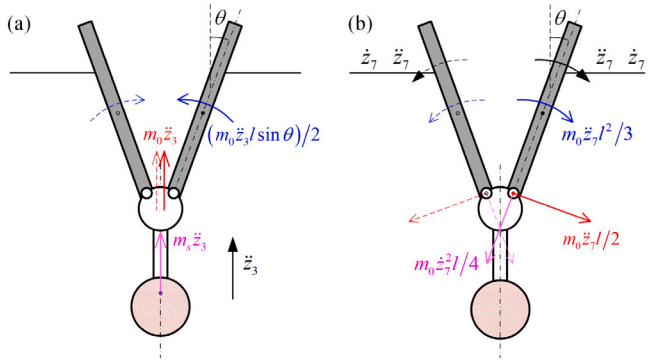

Fig. A.20. (a) Inertial force/moment acting on the device due to acceleration in Mode 3; (b) Inertial force/moment acting on the device due to acceleration in Mode 7.

Fig. A.20 illustrates the schematic diagram of inertial force/moment acting on the C-WEC due to accelerations in Modes 3 and 7. Fig. A.20a demonstrates

$$m_{3,3}^{(0)} = m_s + 2m_0 = m, \tag{A.5}$$

and

$$m_{7,3}^{(0)} = -m_0 l \sin\theta. \tag{A.6}$$

As indicated in Fig. A.20b, we have

$$m_{7,7}^{(0)} = \frac{2m_0 l^2}{3} = 2I, \tag{A.7}$$

and

$$m_{3,7}^{(0)} = -m_0 l \sin\theta - \frac{m_0 l \dot{z}_7^2 \cos\theta}{2\ddot{z}_7} \approx -m_0 l \sin\theta, \tag{A.8}$$

in which the $\dot{z}_7^2$ associated term is neglected in this paper provided the motion response is assumed to be small.

References

[1] A. Clément, P. McCullen, A.F.d.O. Falcão, A. Fiorentino, F. Gardner, K. Hammarlund, G. Lemonis, T. Lewis, K. Nielsen, S. Petroncini, M.T. Pontes, P. Schild, B.O. Sjöström, H.C. Sørensen, T. Thorpe, Wave energy in Europe: current status and perspectives, Renew. Sustain. Energy Rev. 6 (5) (2002) 405–431.

[2] R. Gomes, J. Henriques, L. Gato, A. Falcão, Time-domain simulation of a slack-moored floating oscillating water column and validation with physical model tests, Renew. Energy 149 (2020) 165–180.

[3] Z. Liu, C. Xu, N. Qu, Y. Cui, K. Kim, Overall performance evaluation of a model-scale OWC wave energy converter, Renew. Energy 149 (2020) 1325–1338.

[4] H. Jin, H. Zhang, D. Xu, D. Jun, S. Ze, Low-frequency energy capture and water wave attenuation of a hybrid WEC-breakwater with nonlinear stiffness, Renew. Energy 196 (2022) 1029–1047.

[5] A. Li, Y. Liu, X. Wang, Hydrodynamic performance of a horizontal cylinder wave energy converter in front of a partially reflecting vertical wall, Renew. Energy 194 (2022) 1034–1047.

[6] I. Collins, M. Hossain, W. Dettmer, I. Masters, Flexible membrane structures for wave energy harvesting: A review of the developments, materials and computational modelling approaches, Renew. Sustain. Energy Rev. 151 (2021) 111478.

[7] A. Babarit, Ocean Wave Energy Conversion: Resource, Technologies and Performance, Elsevier, 2017.

[8] S. Jin, D. Greaves, Wave energy in the UK: Status review and future perspectives, Renew. Sustain. Energy Rev. 143 (2021) 110932.

[9] J.R. Chaplin, V. Heller, F.J.M. Farley, G.E. Hearn, R.C.T. Rainey, Laboratory testing the Anaconda, Phil. Trans. R. Soc. A 370 (1959) (2012) 403–424.

[10] A. Babarit, J. Singh, C. Mélis, A. Wattez, P. Jean, A linear numerical model for analysing the hydroelastic response of a flexible electroactive wave energy converter, J. Fluids Struct. 74 (2017) 356–384.

[11] M.-R. Alam, Nonlinear analysis of an actuated seafloor-mounted carpet for a high-performance wave energy extraction, Proc. R. Soc. A 468 (2146) (2012) 3153–3171.

[12] S. Michele, F. Buriani, E. Renzi, M. van Rooij, B. Jayawardhana, A.I. Vakis, Wave energy extraction by flexible floaters, Energies 13 (23) (2020) 6167.

[13] S. Michele, S. Zheng, D. Greaves, Wave energy extraction from a floating flexible circular plate, Ocean Eng. 245 (2022) 110275.

[14] S. Zheng, S. Michele, H. Liang, M. Meylan, D. Greaves, Wave power extraction from a floating elastic disk-shaped wave energy converter, J. Fluid Mech. 948 (2022) A38.

[15] E. Renzi, S. Michele, S. Zheng, S. Jin, D. Greaves, Niche applications and flexible devices for wave energy conversion: A review, Energies 14 (20) (2021) 6537.

[16] F. Farley, The free floating clam - a new wave energy converter, in: 9th European Wave and Tidal Energy Conference (EWTEC), Southampton, UK, 2011.

[17] J. Phillips, D. Greaves, A. Raby, The free floating Clam– performance and potential, in: 11th European Wave and Tidal Energy Conference (EWTEC), Nantes, France, 2015.

[18] J. Phillips, Mathematical and Physical Modelling of a Floating Clam–Type Wave Energy Converter (Ph.D. thesis), University of Plymouth, 2016.

[19] A. Kurniawan, J.R. Chaplin, D.M. Greaves, M. Hann, Wave energy absorption by a floating air bag, J. Fluid Mech. 812 (2017) 294–320.

[20] A. Kurniawan, J. Chaplin, M. Hann, D. Greaves, F. Farley, Wave energy absorption by a submerged air bag connected to a rigid float, Proc. R. Soc. A 473 (2200) (2017) 20160861.

[21] G. Moretti, G. Rosati Papini, L. Daniele, D. Forehand, D. Ingram, R. Vertechy, M. Fontana, Modelling and testing of a wave energy converter based on dielectric elastomer generators, Proc. R. Soc. A 475 (2222) (2019) 20180566.

[22] T. Asai, K. Sugiura, Numerical evaluation of a two-body point absorber wave energy converter with a tuned inerter, Renew. Energy 171 (2021) 217–226.

[23] E. Faraggiana, C. Whitlam, J. Chapman, A. Hillis, J. Roesner, M. Hann, D. Greaves, Y.-H. Yu, K. Ruehl, I. Masters, G. Foster, G. Stockman, Computational modelling and experimental tank testing of the multi float WaveSub under regular wave forcing, Renew. Energy 152 (2020) 892–909.

[24] A. Falcão, P. Justino, J. Henriques, J. André, Reactive versus latching phase control of a two-body heaving wave energy converter, in: 2009 European Control Conference (ECC), 2009, pp. 3731–3736.

[25] X. Zhang, J. Yang, Power capture performance of an oscillating-body WEC with nonlinear snap through PTO systems in irregular waves, Appl. Ocean Res. 52 (2015) 261–273.

[26] J. Todalshaug, G. Ásgeirsson, E. Hjálmarsson, J. Maillet, P. Möller, P. Pires, M. Guérinel, M. Lopes, Tank testing of an inherently phase-controlled wave energy converter, Int. J. Mar. Energy 15 (2016) 68–84.

[27] R. Harne, M. Schoemaker, B. Dussault, K. Wang, Wave heave energy conversion using modular multistability, Appl. Energy 130 (2014) 148–156.

[28] H. Zhang, R. Xi, D. Xu, K. Wang, Q. Shi, H. Zhao, B. Wu, Efficiency enhancement of a point wave energy converter with a magnetic bistable mechanism, Energy 181 (2019) 1152–1165.

[29] S. Zheng, Y. Zhang, G. Iglesias, Concept and performance of a novel wave energy converter: Variable Aperture Point–Absorber (VAPA), Renew. Energy 153 (2020) 681–700.

[30] S. Jin, S. Zheng, D. Greaves, On the scalability of wave energy converters, Ocean Eng. 243 (2022) 110212.

[31] D. Evans, Maximum wave-power absorption under motion constraints, Appl. Ocean Res. 3 (4) (1981) 200–203.

[32] S. Zheng, Y. Zhang, Analysis for wave power capture capacity of two interconnected floats in regular waves, J. Fluids Struct. 75 (2017) 158–173.

[33] J. Falnes, Ocean Waves and Oscillating Systems: Linear Interactions Including Wave–Energy Extraction, Cambridge University Press, 2002.